Nano Research 2016, 9(2): 329–343
DOI 10.1007/s12274-015-0912-x
Research Article
ISSN 1998-0124
CN 11-5974/O4

Small-sized tungsten nitride anchoring into a 3D CNT-rGO framework as a superior bifunctional catalyst for the methanol oxidation and oxygen reduction reactions

Haijing Yan, Meichen Meng, Lei Wang, Aiping Wu, Chungui Tian (✉), Lu Zhao, and Honggang Fu (✉)

Key Laboratory of Functional Inorganic Material Chemistry, Ministry of Education of the People's Republic of China, Heilongjiang University, Harbin 150080, China

Received: 22 July 2015
Revised: 17 September 2015
Accepted: 5 October 2015

KEYWORDS
small-sized tungsten nitride,
3D CNT-rGO,
bifunctional catalyst,
methanol oxidation reaction,
oxygen reduction reaction

ABSTRACT

The application of direct methanol fuel cells (DMFC) is hampered by high cost, low activity, and poor CO tolerance by the Pt catalyst. Herein, we designed a fancy 3D hybrid by anchoring tungsten nitride (WN) nanoparticles (NPs), of about 3 nm in size, into a 3D carbon nanotube-reduced graphene oxide framework (CNT-rGO) using an assembly route. After depositing Pt, the contacted and strongly coupled Pt–WN NPs were formed, resulting in electron transfer from Pt to WN. The 3D Pt–WN/CNT-rGO hybrid can be used as a bifunctional electrocatalyst for both methanol oxidation reaction (MOR) and oxygen reduction reaction (ORR). In MOR, the catalysts showed excellent CO tolerance and a high mass activity of 702.4 $mA \cdot mg_{Pt}^{-1}$, 2.44 and 3.81 times higher than those of Pt/CNT-rGO and Pt/C(JM) catalysts, respectively. The catalyst also exhibited a more positive onset potential (1.03 V), higher mass activity (151.3 $mA \cdot mg_{Pt}^{-1}$), and better cyclic stability and tolerance in MOR than ORR. The catalyst mainly exhibited a 4e-transfer mechanism with a low peroxide yield. The high activity was closely related to hybrid structure. That is, the 3D framework provided a favorable path for mass-transfer, the CNT-rGO support was favorable for charge transfer, and strongly coupled Pt–WN can enhance the catalytic activity and CO-tolerance of Pt. Pt–WN/CNT-rGO represents a new 3D catalytic platform that is promising as an electrocatalyst for DMFC because it can catalyze both ORR and MOR in an acidic medium with good stability and highly efficient Pt utilization.

1 Introduction

Proton exchange membrane fuel cells (PEMFCs) are promising devices for converting chemical energy into electrical energy with high theoretical efficiency [1]. Among them, the direct methanol fuel cell (DMFC) has attracted vast attention due to its low cost and safe, easy storage and transfer of liquid methanol [2].

Address correspondence to Chungui Tian, chunguitianhq@163.com; Honggang Fu, fuhg@vip.sina.com

Robust catalysts are required in both the anode (methanol oxidation reaction, MOR) and cathode (oxygen reduction reaction, ORR) for the DMFC to work with high efficiency. Pt metal is the current state-of-the-art catalytic material. However, MOR and ORR both suffer from low stability, low Pt catalyst activity, and slow kinetics [3, 4]. After long-term operation, migration and aggregation of the catalyst to form large particles, and poisoning by intermediates, such as CO, can result in a decrease in catalytic activity [3]. Moreover, due to the sluggishness of ORR at the cathode, a large amount of Pt catalyst is required to achieve a reasonable overpotential at realistic current densities matching the anode [5]. The large usage, high cost, and decrease in activity of Pt over time has driven an intensive search for the stable, low Pt, or even Pt-free, catalysts to make DMFC commercially viable.

Many strategies have been proposed to make advanced catalysts for MOR and ORR. For MOR, the total replacement of Pt is impossible due to the low stability of non-Pt, cheap metals in an acidic medium [6]. The catalytic reaction proceeds via different routes in alkaline and acid media. Generally, the activity of Pt catalysts can be modified by changing their size, morphology, improving their dispersion, and exposing the "high-energy" plane, as well as alloying with cheap metals [7–11]. These strategies are also suitable for improving the performance of Pt-based catalysts in ORR. However, in practical applications, these Pt-based catalysts still suffer from migration and aggregation to form large particles, and losing the active "high-energy" plane over time in MOR [9–11]. Additionally, Pt catalysts are susceptible to CO poisoning, with limited enhancements in mass activity. The use of Pt-based alloys can decrease the amount of Pt metal used and improve CO tolerance, but the cheaper metals in the alloy dissolve easily during the reaction. This would result in a decrease in catalytic activity during long operation [9–11]. The problems of using Pt and Pt-based alloys in ORR are similar to those for MOR [12–13]. Recently, non-noble metals and metal-free catalysts, such as N, P, and S-doped carbon, C_3N_4, and polymers, have been demonstrated as low-cost catalysts for ORR [14–18]. Unlike MOR, this allows Pt metal to be completely replaced with a cheaper catalyst in ORR. However, low cost non-noble metal and metal-free catalysts have suffered from either low conductivity or low activity in ORR [19–21]. More importantly, these catalysts usually show inferior catalytic activity in an acid medium, and are only suitable for use in alkaline electrolytes. Currently, membranes suitable for acid electrolytes have relatively perfect preparative techniques, while techniques for alkaline membranes are relatively absent [22]. Thus, there are problems in selecting suitable membranes to accompany low cost, non-noble metal catalysts. This inconsistency in anode and cathode catalysts also makes the assembly of fuel cells inconvenient. Therefore, it is necessary to explore bifunctional catalysts with low costs (using of low amount of Pt), good activity, and high stability that catalyze both the ORR and MOR in an acidic medium.

The use of suitable co-catalysts is a way to potentially solve the problem. Transition metal nitrides and carbides have attracted considerable interest in the field of DMFCs because of their unique Pt-like properties [23]. Various examples, such as WC, Mo_2C, VN, and WN, have been designed as co-catalysts for MOR and ORR [24–27]. To fully explore the potential of nitrides as co-catalysts, several qualities have to be present: i) A suitable support, with good conductivity for a quick charge-transfer rate, should be adopted to anchor the nitrides with good dispersion; ii) the catalyst (or carriers) should be porous for easy and fast mass-transfer; and iii) the nitride particle sizes should be as small as possible to increase the chance of nitrides contacting the Pt catalyst to promote the synergistic effect. Carbon nanotubes (CNT), graphene, and carbon black have been used as nitride supports (carbides), but usually suffer from large sizes and poor nitride dispersion on the support [24, 25, 27]. Also, the supports have either low-conductivity or a small BET surface (or low porosity), which are not favorable for a quick charge-transfer rate or fast mass-transfer in electrocatalytic reactions. Recently, we have demonstrated that small and highly dispersed WN nanoparticles (NPs) can be anchored to reduced graphene oxide (rGO) using polyoxometalate clusters as a W source [27]. It is known that defects in GO are difficult to recover, which lead to a lower conductivity in rGO [28]. This has limited the full utilization of graphene's advantages as a support.

If a "pillar" with good conductivity is placed between rGO layers, a 3D support would be constructed that would impede the aggregation of GO. The construction of the 3D architectures (such as a 3D pore carbon network) is considered an efficient way to facilitate ion transport in electrochemical reactions, thus enhancing the application performance of the materials [29–32]. A 1D CNT is the ideal pillar due to having a 1D structure and better conductivity than rGO. Thus, the hybrid structure of 2D graphene with a 1D CNT was proposed as a better support for WN than either CNT or rGO due to the combined advantages of CNT conductivity and the 2D plane structure of graphene. Importantly, the space of adjacent graphene separated by a CNT can provide large, accessible, multi-sized pores for fast transportation of reactants to active sites. It is expected that the loading of small WN particles into a 3D CNT-rGO hybrid has the potential to produce an advanced support. The CNT can endow the hybrid with good conductivity for good transfer-charge, while the plane structure of graphene favors uniform loading of NPs. WN can improve the catalytic activity of Pt through a synergistic catalytic effect.

Herein, we report the construction of a 3D electrocatalyst by anchoring WN NPs with small-sizes (ca. 3 nm) into 3D CNT-rGO hybrids (WN/CNT-rGO) based on an assembly route. After loading Pt, the 3D Pt–WN/CNT-rGO was used as a catalyst for MOR and ORR. It was found that 3D Pt–WN/CNT-rGO containing ca. 8% Pt by mass showed enhanced performance with remarkable catalytic activity, good CO tolerance, and stability towards MOR and ORR. The mass activity of 3D Pt–WN/CNT-rGO was about 702.4 $mA \cdot mg_{Pt}^{-1}$, which is 2.44 and 3.81 times those of Pt/CNT-rGO and commercial Pt/C(JM) in MOR. For ORR, the 3D catalyst exhibited a more positive onset potential (1.03 V) and long-term stability. In addition, the mass activity for 3D Pt–WN/CNT-rGO (151 $mA \cdot mg_{Pt}^{-1}$) was higher than that of Pt/CNT-rGO (94 $mA \cdot mg_{Pt}^{-1}$) and Pt/C(JM) (64 $mA \cdot mg_{Pt}^{-1}$). The excellent performance of 3D Pt–WN/CNT-rGO was attributed to the coefficient results of 0D WN and 3D CNT-rGO, in which 0D WN played a role in improving catalytic activity and CO tolerance, while 3D CNT-rGO was of great importance in raising the ion diffusion and conductivity of the whole catalyst.

2 Experimental

2.1 Material synthesis

2.1.1 *Preparation of 3D CNT-GO hybrids chemicals*

$H_4[SiO_4(W_3O_9)_4]$ (SiW_{12}), H_2PtCl_6, and CNTs were purchased from Shenzhen Nanotech Port Co., Ltd. Ethanol (C_2H_5OH) was purchased from Tianjin Kermel Chemical Reagent Co., Ltd. The polyethyleneimine (PEI, M_W: 600,000–1,000,000) was purchased from Fluka. All reagents were used as received without further purification.

To construct the 3D CNT-GO hybrid, GO was first synthesized from graphite by a modified Hummer's method. Functionalized CNT (F-CNT) was prepared as follows: A pristine CNT (5.0 g), HNO_3 (65%, 100 mL, 1.465 mol) and H_2SO_4 (98%, 300 mL, 5.52 mol) were added into a 1,000 mL flask equipped with a condenser under vigorous stirring. The flask was immersed in an ultrasonic bath for 30 min, and then stirred for 30 min under reflux at 80 ℃. This process was repeated 6 times. A dense brown gas was evolved during this period. After cooling to room temperature, the reaction mixture was diluted with 500 mL of deionized (DI) water and then vacuum-filtered through filter paper (Fisher). The solid was dispersed in DI water and filtered again, and then 200 mL of DI water was used to wash the filter cake several times. The dispersion, filtering, and washing steps were repeated until the pH of the filtrate reached to about 7 (at least four cycles were required). The filtered solid was dried under vacuum for 24 h at 60 ℃, affording F-CNT.

To effectively assemble to the F-CNT, GO was modified with positive charge PEI. In detail, the GO sheets (80 mg) were dispersed in water (20 mL) to form a stable dispersion (4 $mg \cdot mL^{-1}$) in an ultrasonic bath for 10 min. The resulting GO dispersion was mixed with PEI aqueous solution (20 mL, 4 $mg \cdot mL^{-1}$) under stirring. After the mixed solution was stirred for 24 h, the excess polymer was removed by repeated centrifugation (4,500 rpm, 5 min) and washing cycles. PEI-GO was dispersed in deionized water (20 mL). F-CNT (40 mg) dispersed in 20 mL deionized water was dropped into the PEI-GO solution (CNT : GO = 1:2) under vigorous stirring. After 24 h, the 3D CNT-GO hybrid was obtained.

2.1.2 The anchoring of small-sized WN on 3D CNT-rGO (3D WN/CNT-rGO)

The WN NPs were anchored on the 3D CNT-GO hybrid with SiW_{12} clusters as a W source though an assembly method. SiW_{12} (0.12 g) cluster dissolved in deionized water (40 mL) was added dropwise into the CNT-GO solution (40 mL, 3 mg·mL^{-1}) under vigorous stirring. After stirring for 24 h, the mixture was transferred into a 100 mL Teflon-lined autoclave and treated at 180 ℃ for 10 h. The resulting black solid was collected by centrifugation, and washed repeatedly with DI water and alcohol. The resulting product was denoted as 3D SiW_{12}/CNT-rGO and dried at 60 ℃ in a vacuum oven for 6 h. The black color indicates the transformation of GO to GO-derived graphene in the hydrothermal reaction. Before nitridation, the SiW_{12}/CNT-rGO was calcined at 300 ℃ for 5 h. After heating at 800 ℃ under NH_3 for 3 h (a heating rate of 5 ℃·min^{-1}) and slow cooling to room temperature under a N_2 atmosphere, 3D WN/CNT-rGO was obtained. The content of WN in WN/CNT-rGO was about 50.3 wt.%, as determined by thermogravimetric analysis (Fig. S1 in the Electronic Supplementary Material (ESM)).

2.1.3 Construction of 3D Pt–WN/CNT-rGO

3D Pt–WN/CNT-rGO was obtained by loading Pt onto the WN/CNT-rGO hybrid by reduction with $NaBH_4$. Typically, 3D WN/CNT-rGO (100 mg) was suspended in deionized water and ultrasonicated to form a dispersed slurry. The slurry was added to H_2PtCl_6 solution with a Pt concentration of 2 mM. NaOH solution was then added to adjust the pH of the suspension to between 8 and 9. An excess of $NaBH_4$ solution was added to the mixture, followed by vigorous stirring for 2–3 h at ambient temperature. Then the product was allowed to settle, collected by filtration, rinsed thoroughly with DI water and dried. The overall content of Pt in Pt–WN/CNT-rGO was ca. 8 wt.%. As a control, CNT-rGO-supported 20 wt.% Pt catalyst (Pt/CNT-rGO) was also prepared. Commercially available 20 wt.% Pt/carbon black (Johnson Matthey), labeled Pt/C(JM), were used as references for comparison.

2.2 Physical characterizations

The structure of the samples was analyzed by scanning electron microscopy (SEM: Hitachi S-4800), with an acceleration voltage of 5 kV, and transmission electron microscopy (TEM: JEM-2100) with an acceleration voltage of 200 kV. Carbon-coated copper grids were used as sample holders for TEM analysis. X-ray diffraction (XRD) patterns were obtained on a Bruker D8 diffractometer using CuKα (λ = 1.5406 Å) radiation. The accelerating voltage and the applied current were 40 kV and 20 mA, respectively. X-ray photoelectron spectroscopy (XPS) analysis was performed on a VG ESCALABMK II with MgKα achromatic X-ray source (1,253.6 eV). Raman measurement was performed with a Jobin Yvon HR 800 micro-Raman spectrometers at 457.9 nm. Thermogravimetric analysis was performed on a TA-Q600 thermal analyzer with a heating rate of 10 K·min^{-1} in air. The N_2 adsorption–desorption isotherms of as-made samples were conducted using a Micromeritics Tristar II. The samples were degassed for 10 h at 150 ℃ under vacuum before the measurements were taken.

2.3 Electrochemical measurements

Methanol electro-oxidation measurements were performed with a BAS100B electrochemical workstation. The conventional three-electrode cell was used for electrochemical testing, in which the Pt plate acted as the counter electrode, a saturated Hg/Hg_2Cl_2 electrode as the reference electrode, and a glassy carbon (GC) electrode with 0.4 cm diameter as the working electrode. Oxygen reduction evaluation was performed with a Pine rotating disk electrode (Pine Inst.).

The working electrode was made from the carbon-supported Pt catalysts (Nafion as a binder). Catalyst (5 mg) was mixed with Nafion ionomer (0.5 mL, 0.5 wt.%) and then dispersed in 1.5 mL of ethanol solution. After the catalyst ink was sonicated for 0.5 h, a volume of 10 μL of the mixture solution was then pipetted onto the GC substrate. For MOR, the cyclic voltammetry (CV) tests were performed in N_2-purged 1 M H_2SO_4 solution, with or without 1 M CH_3OH, at room temperature and at a scan rate of 50 mV·s^{-1}. CO stripping measurement was performed as follows: After purging the solution with N_2 for 20 min, CO was bubbled for 15 min to form a CO adsorbed layer on the catalyst while maintaining the potential at –0.15 V. Excess CO in the solution was purged with N_2 for 20 min and CO stripping curve was recorded

in 1 M H_2SO_4 solution at 20 mV·s^{-1}. Electrochemical impedance spectroscopy (EIS) of the samples was measured in a 1 M H_2SO_4 solution containing 1 M CH_3OH solution over the frequency range 1–10^5 Hz. For ORR, the catalyst was deposited on a rotating disk electrode (0.247 cm^2) and dried at room temperature. The electrochemical tests were performed in an O_2-saturated 0.1 M $HClO_4$ solution and the scan rate was 5 mV·s^{-1}. All electrochemical studies were carried out at 25 ℃.

3 Results and discussion

3.1 Characterization of 3D WN/CNT-rGO and 3D Pt–WN/CNT-rGO

The 3D CNT-GO framework was constructed by inserting 1D CNT pillars into a 2D GO shelf through an electrostatic-assembly method (Fig. 1, step 1). GO has a lot of functional groups with negative charges (hydroxyl and carboxyl). The modification of GO with PEI can endow the GO with positive charge, which is favorable for the assembly of GO with F-CNT pillars [33–37]. The assembly of F-CNT and PEI-GO resulted in the formation of the 3D CNT-GO hybrid. Besides the role in assembling F-CNT with GO, the PEI modification was also necessary to anchor the $H_4[SiO_4(W_3O_9)_4]$ (SiW_{12}) clusters on the support. As we aimed to grow WN on rGO, the modification of PEI was performed on GO, but not F-CNT. The anchoring of SiW_{12} clusters was realized under hydrothermal conditions, which also simultaneously reduced GO to rGO (3D SiW_{12}/CNT-rGO). After calcining in air and NH_3 atmospheres in sequence, the 3D WN/CNT-rGO hybrid was formed (Fig. 1, step 2). The hybrids could be used as promising support for Pt in MOR and ORR (Fig. 1, step 3). The formation of 3D framework was verified by SEM and TEM. From SEM images (Fig. 2(a)), both 1D CNT and thin rGO layers could be clearly observed in the WN/CNT-rGO hybrid. The CNT pillars were well-combined with rGO layers, as shown in Fig. 2(b). The tight combination favored improved conductivity in the support, while also preventing rGO aggregation. As a result, separate, thin rGO sheets could be formed (Fig. 2(b) inset), while large, accessible pores could be formed between adjacent rGO separated by CNT,

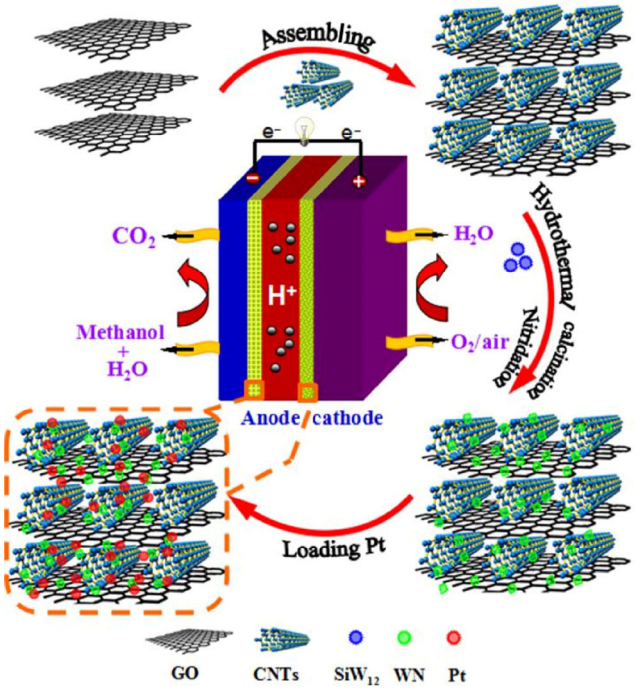

Figure 1 Schematic process used to construct the 3D Pt–WN/CNT-rGO catalyst.

which undoubtedly provided avenues for the fast transportation of reactants to electroactive sites. However, WN particles could not be seen, possibly owing to their small size and good dispersion exceeding the limits of SEM. TEM images of 3D WN/CNT-rGO provided even more exhaustive information. They showed that CNTs 20–40 nm in diameter were well-combined with rGO (Figs. 2(c) and 2(d)). The margin of carbon sheets were about 4 graphite layers in thickness, indicating the formation of thin graphene sheets. The TEM test further verified the formation of a tightly combined CNT and rGO layer, consistent with SEM results. In addition, small particles, with sizes around 3 nm, could be observed on carbon supports with good dispersion. The high-resolution TEM (HRTEM) image (the inset in Fig. 2(e)) showed the distance between two adjacent planes as around 0.25 nm, corresponding to the (100) crystal facet of the cubic WN. The small size and good dispersion of WN NPs were favorable in enhancing their contacted chance with Pt metal after the deposition of Pt. Figures 2(f)–2(h) show the TEM images of 3D Pt–WN/CNT-rGO composites. We can see that the particles of about 3 nm are well distributed on the 3D CNT-rGO. The TEM image in Fig. 2(h) shows small-sized particles in close

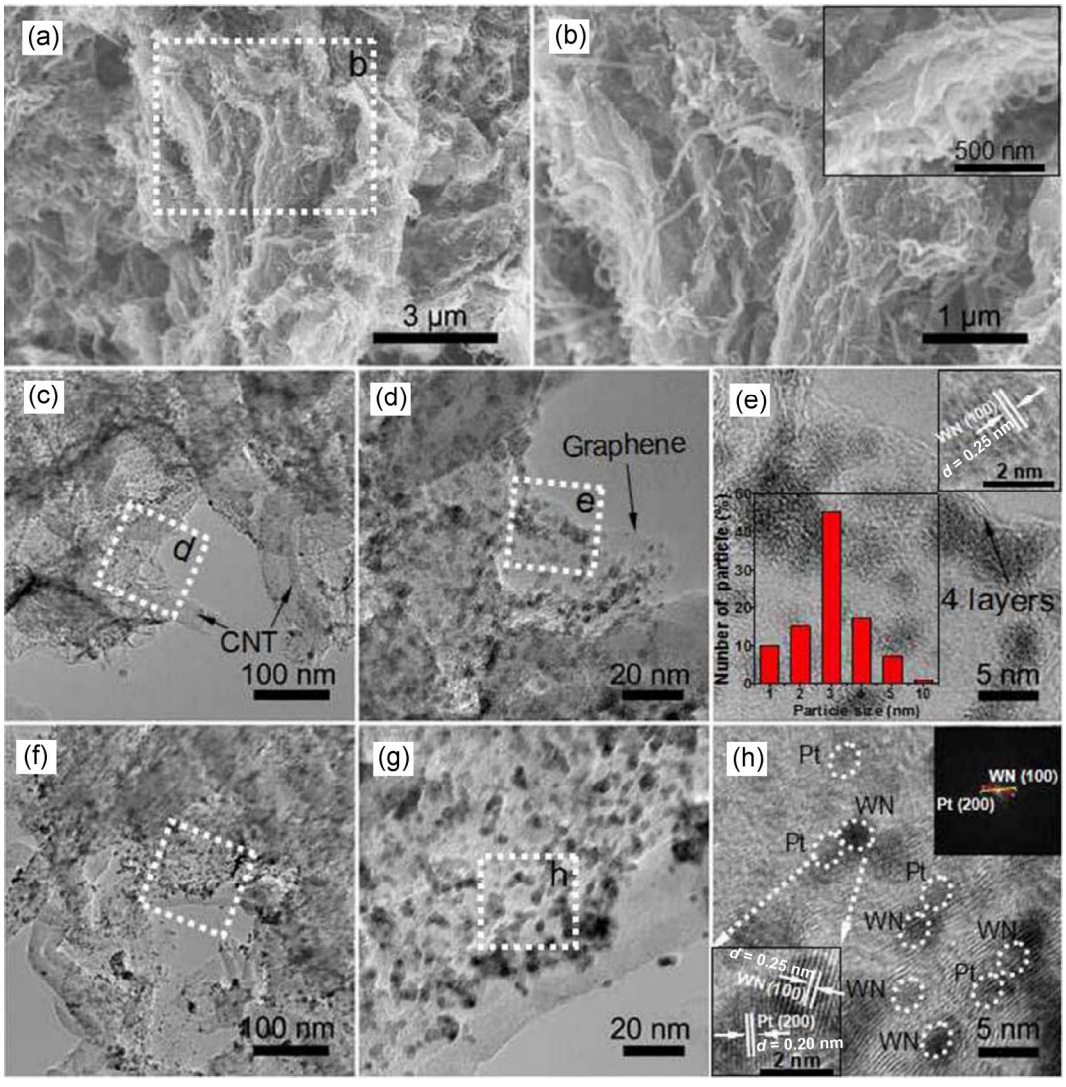

Figure 2 (a)–(b) SEM and (c)–(e) TEM images of 3D WN/ CNT-rGO. The inset in (e) shows the HRTEM and histograms of the WN particles. (f)–(h) TEM images of 3D Pt–WN/CNT-rGO. The inset in (h) is the HRTEM and FFT image of WN and Pt.

contact on the 3D support. This is different with that of WN/CNT-rGO, implying the formation of the contacted WN–Pt. The inset of Fig. 2(f) displays the well-defined lattice fringes of the (100) crystal plane of WN in one area, and the (200) crystal plane of Pt in adjacent areas surrounding WN. The Fast Fourier Transform (FFT) image (Fig. 2(h) inset) shows two distances, 0.008 and 0.0100 pm corresponding to a (100) plane of WN and (200) plane of Pt, and consistent with the HRTEM test. Moreover, the STEM images of 3D Pt–WN/CNT-rGO are also given in Fig. S2 in the ESM, further confirming the homogeneous distribution of C, N, W, and Pt in 3D Pt–WN/CNT-rGO. The tests revealed the formation of intimately contacted Pt and WN NPs, which was largely favored in promoting the "synergistic effect" or WN and Pt in highly effective electrocatalysis.

Charge-transfer and mass-transfer are two key processes in electrocatalytic reactions. The crystallinity of the carbon materials is closely related to their conductivity (charge-transfer ability). The crystallinity of the carbon support in the 3D catalyst was analyzed by Raman spectroscopy (Fig. S3 in the ESM). Two prominent peaks D (about 1,368 cm^{-1}) and G (about 1,590 cm^{-1}) were usually assigned as the breathing mode of *k*-point phonons of A_{1g} symmetry and the E_{2g} phonons of sp^2 carbon atoms, respectively [38]. The intensity ratio of G/D (I_G/I_D) was proportional to the

crystalline degree of carbon materials [39]. Specifically, the I_G/I_D ratios were 1.15 and 1.34 for GO and CNT-GO, respectively. Higher I_G/I_D values for CNT-GO than GO indicated that the introduction of CNT improved crystallization of the carbon support. The increase of I_G/I_D after the formation of 3D SiW_{12}/CNT-rGO can be attributed to the hydrothermal process, which can remove residual oxygenous groups from GO and F-CNT, and thus improve crystallinity in the carbon support. However, the ratio of I_G/I_D decreased after the formation of 3D WN/CNT-rGO, ascribed to the disordered structure induced by intensive interaction of 0D WN and 3D CNT-rGO, as well as the doping of 3D CNT-rGO with N under NH_3 atmosphere [40]. In addition, the I_G/I_D is about 1.12 for WN/CNT-rGO samples, much higher than that of WN/rGO (1.01) [27]. Raman spectra demonstrated that the introduction of CNT can improve the crystallization of the carbon support, thus potentially improving the charge-transfer ability of the materials.

To effectively transfer mass, the catalyst should have large BET specific surface area (S_{BET}) with suitable pores. The SEM test verified the formation of large, accessible pores favorable for mass-transfer. Nitrogen adsorption/desorption was used to measure the S_{BET} of samples. The S_{BET} values for 3D Pt–WN/CNT-rGO, Pt/CNT-rGO, and Pt/C(JM) were about 281.1, 118.5, and 163.9 $m^2 \cdot g^{-1}$, respectively (Fig. S4 and Table S1 in the ESM). 3D Pt–WN/CNT-rGO having a higher S_{BET} than Pt/CNT-rGO indicated the important role of WN in preventing the aggregation of rGO. The S_{BET} of the 3D catalysts was also higher than corresponding Pt–WN/rGO (263.2 $m^2 \cdot g^{-1}$) [27], which could contribute to further preventing aggregation of rGO by CNT. The small amplitude of S_{BET} increases may be due to the formation of larger pores in 3D Pt–WN/CNT-rGO. The presence of large pores was favorable for the transfer of liquid electrolytes. We also tested the S_{BET} of Pt/CNT (about 61.1 $m^2 \cdot g^{-1}$) and Pt/rGO (about 50.4 $m^2 \cdot g^{-1}$). The S_{BET} of Pt/CNT-rGO was larger than the sum of Pt/CNT and Pt/rGO, verifying the important role of rational combination of CNT and rGO to improve S_{BET}. The CNT pillars bracing in the graphene shelf can prevent graphene from congregating and provide the large, accessible pores. Overall, the above analyses verified that, by combining a 1D CNT with rGO, a robust 3D catalyst with good conductivity and the large accessible interfaces (pores) was constructed. These characteristics are significantly beneficial for the mass-transfer and charge-transfer of the catalyst in electrocatalytic reactions.

The synergistic effect of WN and Pt is key for promoting the catalytic activity and stability of Pt metal. TEM tests verified the formation of contacted Pt–WN NPs, which were favorable for the development of synergistic effects. The synergistic effect, and thus induced electron transfer, could be proven directly by XPS. As shown in Fig. 3(a), peaks belonging to C, O, N, W, and Pt can clearly be seen in the wide scan spectra. The W4f spectra showed that W from WN was the predominate component in 3D Pt–WN/CNT-rGO. The peaks of W and WN were located at 35.5 and 37.6 eV, respectively, in 3D Pt–WN/CNT-rGO (Fig. 3(b)), while the binding energies (BE) of W4f in WN/CNT-rGO were 35.7 and 37.8 eV, respectively. We can see a negative shift of 0.2 eV by comparing the former with the latter. This interaction was also reflected in the comparison of the Pt spectra of 3D Pt–WN/CNT-rGO and Pt/CNT-rGO (Fig. 3(c)). As shown, the Pt4f spectra for 3D Pt–WN/CNT-rGO and Pt/rGO-CNT showed doublet binding energies of 71.8 ($Pt4f_{7/2}$) and 75.1 eV ($Pt4f_{5/2}$), and 71.4 eV ($Pt4f_{7/2}$) and 74.7 eV ($Pt4f_{5/2}$), respectively, demonstrating a positive shift of 0.4 eV for Pt/rGO-CNT. The BE shift of W4f and Pt4f can be explained by electron transfer from Pt to WN due to close contact and intensive interaction.

The C and N spectra have also been analyzed to give some insight into the structure of Pt–WN/CNT-rGO. The C1s spectrum could be deconvoluted into five sub-peaks, labeled I, II, III, IV, and V, as shown in Fig. 3(d). Peak I represented graphitic carbon with C–C, C=C, and C–H bonds at a BE of 284.6 eV. Four small peaks at higher binding energies indicated the existence of carbon combined with nitrogen and oxygen groups [41]. Specifically, Peak II (285.5 eV) was ascribed to carbon in C–N bonds [42]. The formation of C–N bonds was due to the reaction of NH_3 with carbon. This indicated that NH_3 could react both with W to form N–W bonds and with C, resulting in N doping during the nitriding process. It has been demonstrated that N doping of carbon can improve the electrocatalytic ability of materials [26, 43–45]. So, the formation of

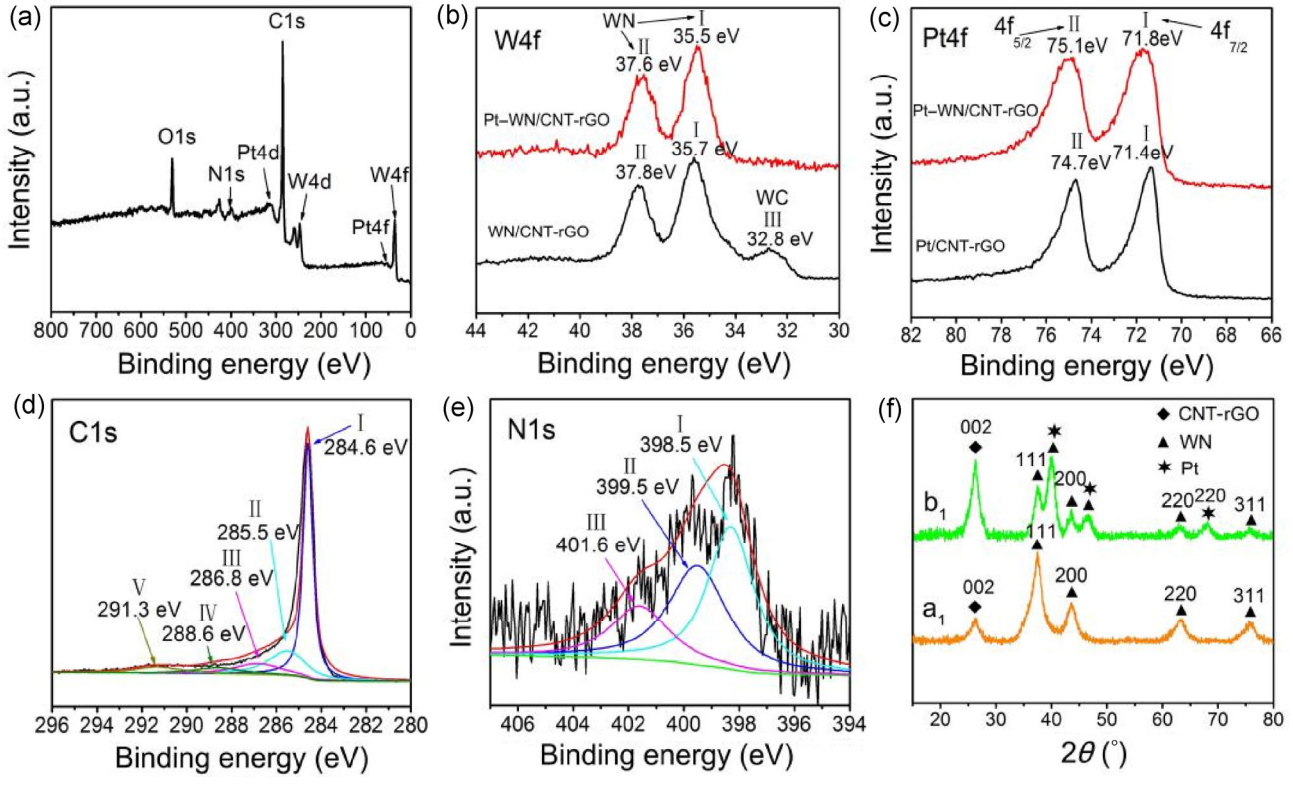

Figure 3 XPS spectra of 3D Pt–WN/CNT-rGO catalyst: (a) wide scan; (b) W4f of 3D WN/CNT-rGO and 3D Pt–WN/CNT-rGO; (c) Pt4f of Pt/CNT-rGO and 3D Pt–WN/CNT-rGO; (d) C1s, (e) N1s, and (f) XRD patterns of (a_1) 3D WN/CNT-rGO and (b_1) 3D Pt–WN/CNT-rGO.

N-doping carbon was favorable for improving the application performance of WN/CNT-rGO. Peaks III, IV, and V were indexed as C–O bonds (286.8 eV), C=O bonds (288.6 eV), and carboxyl groups (O=C–O) (291.3 eV), respectively [42]. As shown, carbon combined with O in the original CNT-GO had much higher peaks than for 3D Pt–WN/CNT-rGO (Fig. S5 in the ESM). The result indicated that oxygen-containing groups in 3D CNT-rGO were removed during preparation. The N1s spectrum (Fig. 3(d)) could be deconvoluted into three peaks. Peak I (398.5 eV) was ascribed to N from WN. Peaks II (399.5 eV) and III (401.6 eV) were derived from N atoms combined with C atoms in graphene. In detail, Peak II can be assigned to pyrrolic/pyridine N, and Peak III to quaternary N [46]. The results from the N spectra are consistent with the carbon spectra. This also implies nitrogen doping on the CNT-rGO has occurred, consistent with the Raman analyses. The interaction could also be reflected in XRD tests. In the XRD patterns of 3D WN/CNT-rGO and 3D Pt–WN/CNT-rGO, the peak at 26.5° was characteristic of (002) planes of the graphitic carbon (CNT-rGO). The diffractions located at 37.6°, 43.8°, 63.7°, and 76.5° were assigned to the (111), (200), (220), and (311) reflections of the cubic WN phase, respectively. For Pt–WN/CNT-rGO, the peaks located at 39.7°, 46.2°, and 67.5° were identified as the (111), (200), and (220) reflections of a face-centered cubic (fcc) structured Pt, respectively, with the peaks belonging to WN weakened for the ternary composites. Similar results were also observed for Pt–WC/carbon and Pt–Mo_2C/carbon [47, 48]. These observations could be explained by intensive interaction of Pt with WN NPs and epitaxial growth of Pt on WN due to the similar electronic structures [23]. The interaction between Pt and WN was more advantageous for application in advanced areas. Moreover, the peak at 26.5° rose remarkably, as shown in Pt–WN/CNT-rGO, which was a result of loading Pt by the $NaBH_4$ method. As demonstrated in other research, the conjugated graphene network (sp^2 carbon) was reestablished when oxygenated groups were removed by chemical

reduction. Meanwhile, the size of the reestablished graphene network becomes smaller than the original, which consequently leads to the increasing intensity ratio of XRD [39]. Thus, after Pt deposition, the carbon peaks clearly increase.

3.2 Electrochemical test

Inconsistencies in anode and cathode catalysts can make fuel cell assembly largely inconvenient, which is unfavorable for applications of fuel cells. It is desirable that the same catalyst can be used for both ORR and MOR in an acidic medium. The electrochemical performance of 3D Pt–WN/CNT-rGO for MOR was evaluated first. Figure 4(a) shows the CV curves recorded in N_2-purged 1.0 M H_2SO_4 containing 1.0 M CH_3OH for methanol electro-oxidation. The current densities of 3D Pt–WN/CNT-rGO, Pt/CNT-rGO, and Pt/C(JM) were 702.4 $mA{\cdot}mg_{Pt}^{-1}$ at 0.64 V, 288.3 $mA{\cdot}mg_{Pt}^{-1}$ at 0.71 V, and 184.5 $mA{\cdot}mg_{Pt}^{-1}$ at 0.65 V, respectively. It was clear to see that 3D Pt–WN/CNT-rGO had given the highest current density, which was 2.44 and 3.81 times higher than those of Pt/CNT-rGO and Pt/C(JM), respectively. The ratio of the forward anodic peak current density (I_f) to the backward anodic peak current density (I_b), I_f/I_b, could be used to indicate the CO tolerance of the catalyst, with a higher I_f/I_b ratio indicating a better CO tolerance [49]. The I_f/I_b for 3D Pt–WN/CNT-rGO was about 1.55, much higher than the 0.92 for Pt/CNT-rGO or 0.77 for Pt/C(JM). The onset potential is also related to the breaking of C–H bonds and subsequent removal of CO by oxidation with OH_{ads} species [50]. The 3D Pt–WN/CNT-rGO catalyst gave the lowest onset potential of 0.18 V, while values for Pt/CNT-rGO and Pt/C(JM) were 0.47 and 0.42 V, respectively. In the electrochemical environment, WC partially changes to a mixture of W(V/VI) oxides, which promotes the dissociation of H_2O into H^+ and OH^-, and provided OH_{ads} to Pt sites [51]. Similar effects have also been observed with WN. Therefore, the excellent CO tolerance was attributed to the activity of WN particles in the decomposition of water, and providing the OH_{ads} species to oxidize the adsorbed CO on Pt surfaces. Figure 4(b) shows the CV curves of the catalysts recorded in N_2-purged 1.0 M H_2SO_4. The electrochemically active surface area (ECSA) of 3D Pt–WN/CNT-rGO was calculated to be 85.21 $m^2{\cdot}g_{Pt}^{-1}$, which is 1.74 and 1.15 times higher than those of Pt/CNT-rGO (48.91 $m^2{\cdot}g_{Pt}^{-1}$) and Pt/C(JM) (74.33 $m^2{\cdot}g_{Pt}^{-1}$), respectively. This can be explained by the well dispersion of Pt and WN NPs anchored into the 3D CNT-rGO supports. The small size of Pt particles also contributed to the large ECSA. Besides, the specific activities (normalized to the ECSA) of 3D Pt–WN/CNT-rGO, Pt/CNT-rGO, and Pt/C(JM) were 8.24, 5.38, and 2.48 $A{\cdot}m_{Pt}^{-2}$, respectively (Fig. 4(c) and Table S2 in the ESM). 3D Pt–WN/CNT-rGO had also given a higher specific activity. The excellent CO tolerance of Pt–WN/CNT-rGO was further demonstrated by CO stripping tests in 1 M H_2SO_4 at room temperature (Fig. 4(d)). 3D Pt–WN/CNT-rGO had the lowest peak potential of 0.57 V, which was more negative than Pt/CNT-rGO (0.61 V, 40 mV shift) and Pt/C(JM) (0.66 V, 90 mV shift). Electrochemical impedance spectroscopy (EIS) is effective at giving information on charge transfer resistance [52]. The semicircle in EIS curves represents MOR charge transfer resistance (R_{ct}), it can be clearly seen from Fig. 4(e) that the corresponding R_{ct} for 3D Pt–WN/CNT-rGO is the smallest among the three catalysts at the potential investigated. This indicated that MOR on the 3D Pt–WN/CNT-rGO catalyst was more favorable than for the other two catalysts, due to a smaller transfer resistance and enhanced reaction kinetics. The results were in good agreement with the mass-transfer and charge-transfer abilities of 3D Pt–WN/CNT-rGO. The stability of the catalyst was reflected in continuous CV tests (Fig. S6 in the ESM). The forward anodic peak had no obvious shift for 3D Pt–WN/CNT-rGO catalyst after 100 CV cycles. In contrast, positive shifts of 9 mV for Pt/CNT-rGO and 14 mV for Pt/C(JM) were clearly observed. The normalization of the initial forward peak current density of 3D Pt–WN/CNT-rGO decreased by about 18.5% after 100 CV cycles, whereas Pt/CNT-rGO and Pt/(JM) lost about 34.9% and 43.3% of their initial current densities, respectively (Fig. 4(f)). These tests confirmed the excellent stability of 3D Pt–WN/CNT-rGO. Chronoamperometric (CA) measurement was also used to test the durability of catalysts. As shown in Fig. S7 in the ESM, normalized decay, corresponding to the current at 15,000 s and initially ($I_{15,000s}/I_{initial}$), was 0.041 for 3D Pt–WN/CNT-rGO, 0.013 for Pt/CNT-rGO,

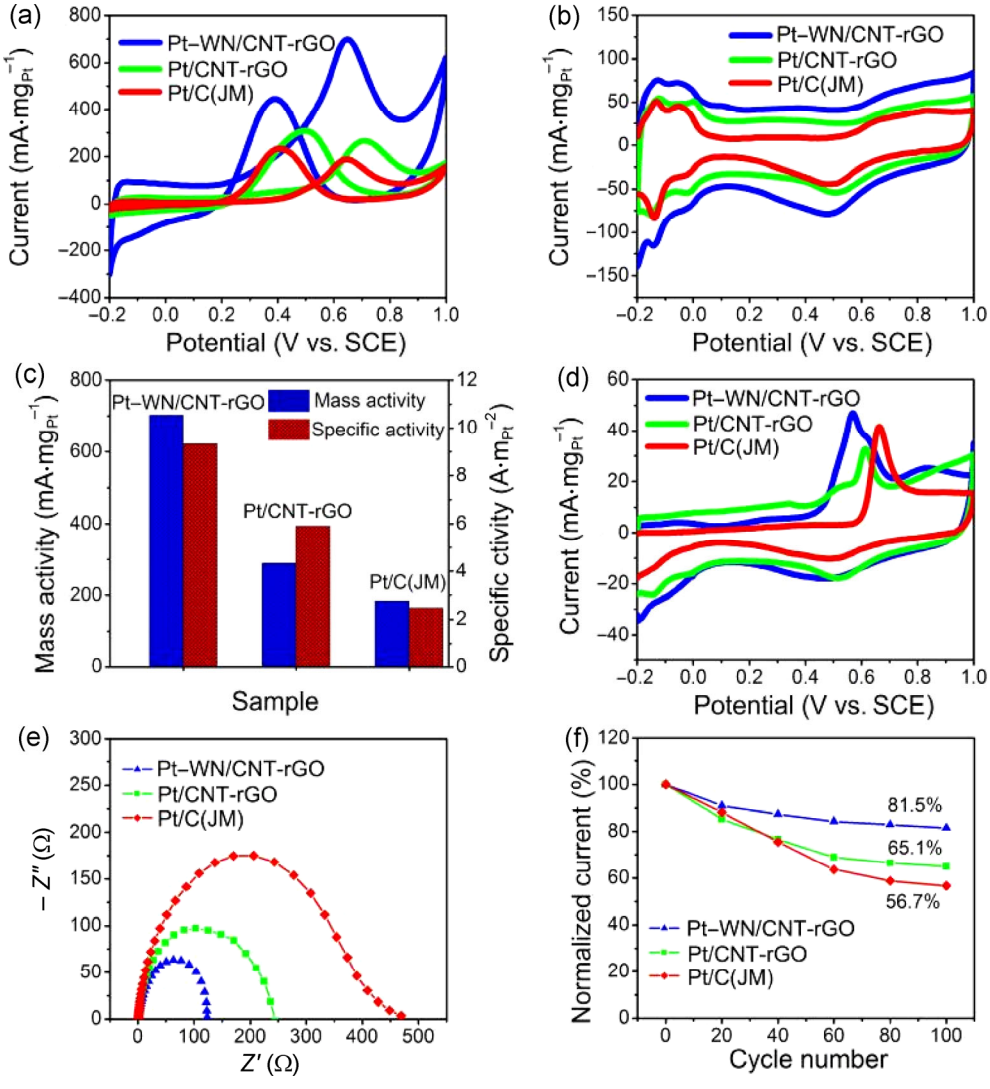

Figure 4 (a) Methanol electro-oxidation curves for different catalysts recorded in aqueous 1 M H_2SO_4 and 1 M CH_3OH solution with a sweep rate of 50 mV·s^{-1}. (b) CV curves recorded in N_2-purged 1 M aqueous H_2SO_4 with a sweep rate of 50 mV·s^{-1}. (c) Mass activity and specific activity for catalysts. (d) CO-stripping curves of the electrodes modified with different catalysts in N_2-protecting 1 M H_2SO_4 solution at a scan rate of 20 mV·s^{-1}. (e) Nyquist plots of EIS for catalysts in 1 M H_2SO_4 and 1 M CH_3OH solution. (f) The forward peak currents of the Pt–WN/CNT-rGO, Pt/CNT-rGO, and Pt/C(JM) catalysts as a function of the number of potential scanning cycles, revealing the best cycling stability for 3D Pt–WN/CNT-rGO.

and 0.0005 for Pt/C(JM).

The much-improved stability could be attributed to the strong interactions between Pt and WN that prevent small Pt particles from falling off and aggregating during methanol oxidation. Moreover, 3D CNT-rGO can prevent graphene from congregating and increasing the mass/charge-transfer ability. The excellent synergistic effect of Pt and WN, and the combined functions of the four constituents (Pt, WN, rGO, and CNT), made 3D Pt–WN/CNT-rGO show such high catalytic activity. Thus, a smaller amount of Pt was required to generate more current, saving a substantial amount of noble metal. Therefore, the obtained Pt–WN/CNT-rGO catalyst should be more suitable for practical application in fuel cell.

In order to investigate the catalytic performance of the 3D electrocatalyst in the ORR, rotating disk electrode (RDE) experiments were performed in O_2-saturated 0.1 M·$HClO_4$ solutions with a scan rate of 5 mV·s^{-1} and a rotating speed of 1,600 rpm at room temperature (Fig. 5(a)). Bare GC was inactive towards ORR, while the other three catalysts exhibited significant

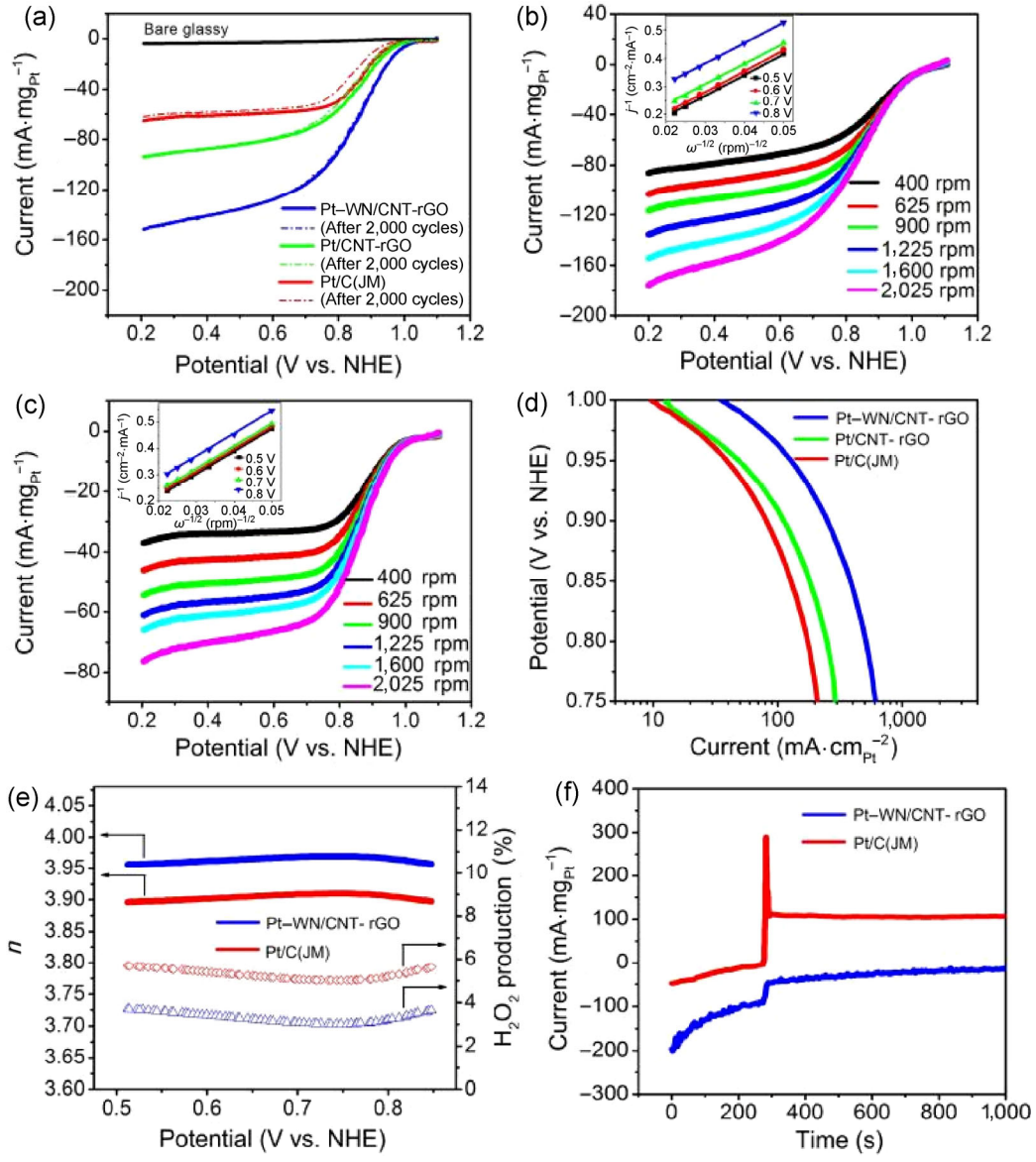

Figure 5 (a) RDE voltammograms for ORR on 3D Pt–WN/CNT-rGO, Pt/CNT-rGO, Pt/C(JM), and bare GC at a 5 mV·s^{-1} scan rate 1,600 rpm in O_2-saturated 0.1 M $HClO_4$ electrolyte. (b) and (c) RDE voltammograms at a 5 mV·s^{-1} scan rate in O_2-saturated 0.1 M $HClO_4$ electrolyte for 3D Pt–WN/CNT-rGO and Pt/C(JM); Koutecky–Levich plots at various potentials used to extract kinetic RDE current are inset (b)–(c). (d) Corresponding Tafel plots of the mass activity–potential curve for ORR. (e) Percentage of peroxide and electron-transfer number (*n*) at various potentials, based on the corresponding RRDE. (f) Methanol tolerance experiments conducted at 0.85 V (vs. NHE) with O_2 bubbling. 1 mL methanol was injected in the electrolyte at 300 s.

catalytic activity. The polarization curves of all carbon-supported catalysts exhibited two distinguishable potential regions, corresponding to well-defined diffusion limiting currents (0.2–0.7 V) followed by a mixed kinetic-diffusion control region (0.7–0.95 V). The onset potential for 3D Pt–WN/CNT-rGO (1.03 V vs. NHE) was higher than those of Pt/CNT-rGO (1.00 V vs. NHE) and Pt/C(JM) (0.98 V vs. NHE), indicating that the introduction of WN greatly improves the activity of the Pt catalyst in ORR. The limiting currents for 3D Pt–WN/CNT-rGO, Pt/CNT-rGO, and Pt/C(JM) were around 151.3, 94.6, and 64.2 mA·mg$_{Pt}^{-1}$, respectively. It can be concluded that 3D Pt–WN/CNT-rGO exhibits superior ORR mass activity to Pt/CNT-rGO and Pt/C(JM). Table S2 in the ESM summarizes the electrochemical data of ORR over the different catalysts used,

further demonstrating the good ORR activity of the 3D Pt–WN/CNT-rGO catalyst. The polarization curves of 3D Pt–WN/CNT-rGO and Pt/C(JM) were recorded at different rotating rates (400–2,025 rpm) on the RDE in an O_2-saturated 0.1 M $HClO_4$ aqueous solution at room temperature to provide further information about the ORR mechanism (Figs. 5(b) and 5(c)). It was obvious that catalytic current increased with the electrode rotating rate. Higher current values at higher rotating rates indicated a higher catalyst turnover rate for ORR at the electrode. The corresponding Koutecky–Levich plots (j^{-1} vs. $\omega^{-1/2}$) at several potentials (Figs. 5(b) and 5(c) inset) exhibited good linearity, with the slopes remaining generally constant, suggesting similar electron-transfer numbers in ORR at different potentials [53]. The electron-transfer number was calculated to be 3.9 according to the Koutecky–Levich equation, indicating a four-electron-transfer process. For comparison of the intrinsic activity of catalysts, the Tafel plots derived from the voltammograms (Fig. 5(a)) are shown in Fig. 5(d). Tafel slopes for Pt–WN/CNT-rGO, Pt/CNT-rGO, and Pt/C(JM) are about –55, –59, and –62 mV·decade^{-1}, respectively. The Tafel slope in the region was relative to adsorbed hydroxyl species at the Pt surface (OH_{ads}), which determines the electrode activity to some content [54]. The percentage of peroxide species, with respect to the total oxygen reduction products and the electron-reduction number (n), was calculated from ring RDE curves (Fig. 5(e)). The yield of peroxide species on the 3D Pt–WN/CNT-rGO was about 3% over the measured potential range, lower than that of Pt/C(JM) (about 5%). The average electron-transfer number was about 3.96 from 0.5 to 0.8 V for the 3D Pt–WN/CNT-rGO catalyst, similar to that of Pt/C(JM) (3.9). The results were consistent with those from the Koutecky–Levich plots based on RDE voltammograms. The results indicated that ORR mainly occurs via a 4-electron-reduction pathway in 0.1 M $HClO_4$ electrolyte on the 3D Pt–WN/CNT-rGO catalyst. Mono-metal Pt-based catalysts have a poor capacity for methanol tolerance at the cathode. To address this problem, one strategy was to form alloy catalysts. For example, the alloys Pt–Au or PtPdCo have shown good methanol tolerance [55–56]. This was attributed to the alloy being able to effectively restrict the carbonized intermediate (mainly CO_{ads}) adsorbed on the Pt surface, which was produced by the self-poisoning process of methanol on Pt at the cathode. Moreover, metal carbides (WC) have been reported to have excellent methanol tolerance in ORR [57]. Considering the similar structure of metal nitrides and carbides, it was reasonable that WN could show a good methanol tolerance in ORR. The methanol tolerance abilities of 3D Pt–WN/CNT-rGO and Pt/C(JM) at different potentials were also tested, including 0.6, 0.65, 0.7, 0.75, 0.8, 0.85, and 0.9 V (Fig. S8 in the ESM). Specially, when the potential was close to the half-wave potential (0.85 V) (Fig. 5(f)), the 3D Pt–WN/CNT-rGO showed good methanol tolerance. Stability tests of different catalysts were performed in 0.1 M $HClO_4$ electrolyte at a scan rate of 100 mV·s^{-1} for up to 2,000 cycles with the potential cycling between 0 and 1.2 V. The RDE voltammograms were recorded in O_2-saturated 0.1 M $HClO_4$ electrolyte at 1,600 rpm with a sweep rate of 5 mV·s^{-1}. For 3D Pt–WN/CNT-rGO, the loss of $E_{1/2}$ was negligible after 2,000 cycles (Fig. 5(a)). In contrast, the $E_{1/2}$ of the Pt/CNT-rGO and Pt/C(JM) catalysts degraded by 30 and 40 mV after 2,000 cycles, respectively. The test further demonstrated the excellent stability of the catalyst in ORR. The stability of 3D Pt–WN/CNT-rGO was mainly attributed to the special structure of 3D Pt–WN/CNT-rGO catalyst, in which 0D WN plays a role in enhancing the catalytic activity and stability of the Pt catalyst, and 3D CNT-rGO is of great importance in raising the ion diffusion and electrical conductivity of the whole catalyst. The electrochemical tests indicated that the 3D Pt–WN/CNT-rGO hybrid could be used as superior bifunctional catalyst for MOR and ORR.

4 Conclusions

A 3D WN/CNT-rGO hybrid has been constructed by anchoring WN NPs (about 3 nm in size) into a 3D CNT-rGO framework based on a controllable assembly route. The advantages of the hybrid, including small WN NP size, improved conductivity for faster mass-transfer and larger, accessible pores for easy mass-transfer, give them great potential as a Pt support in electrocatalytic applications. After depositing low amounts of Pt, the contacted and strongly coupled Pt–WN was formed into a 3D Pt–WN/CNT-rGO

catalyst. The 3D Pt–WN/CNT-rGO hybrid can be used as an advanced bifunctional electrocatalyst for both MOR and ORR, exhibiting improved activity, high stability, good CO tolerance, and excellent tolerance in the methanol oxidation reaction. The catalyst mainly exhibits a 4e-transfer mechanism with a low yield of peroxide species for ORR. Pt–WN/CNT-rGO represented a 3D catalytic platform that was a promising electrocatalyst for DMFC as it is capable of catalyzing both ORR and MOR in an acidic medium with highly efficient utilization of Pt and with good stability. The 3D CNT-rGO hybrid may be useful for anchoring other functional components (oxides, polymer, etc.) for applications in the fields of catalysis and supercapacitors.

Acknowledgements

We gratefully acknowledge the support of this research by the Key Program of the National Natural Science Foundation of China (No. 21031001), the National Natural Science Foundation of China (Nos. 21371053, 21571054, and 21401048), Program for Innovative Research Team in University (No. IRT-1237), Special Research Fund for the Doctoral Program of Higher Education of China (No. 20112301110002), the Natural Science Foundation of Heilongjiang Province (No. QC2014C007), China Postdoctoral Science Foundation funded project (No. 2015T80374), and Excellent Youth Foundation of Heilongjiang University.

Electronic Supplementary Material: Supplementary material (the Raman images, XPS spectrum, S_{BET}, XRD pattern, and TG-DSC of products) is available in the online version of this article at http://dx.doi.org/10.1007/s12274-015-0912-x.

References

[1] Debe, M. K. Electrocatalyst approaches and challenges for automotive fuel cells. *Nature* **2012**, *486*, 43–51.

[2] Long, N. V.; Yang, Y.; Thi, C. M.; van Minh, N.; Cao, Y. Q.; Nogami, M. The development of mixture, alloy, and core–shell nanocatalysts with nanomaterial supports for energy conversion in low-temperature fuel cells. *Nano Energy* **2013**, *2*, 636–676.

[3] Tong, Y. Y.; Kim, H. S.; Babu, P. K.; Waszczuk, P.; Wieckowski, A.; Oldfield, E. An NMR investigation of CO tolerance in a Pt/Ru fuel cell catalyst. *J. Am. Chem. Soc.* **2002**, *124*, 468–473.

[4] Fang, B. Z.; Chaudhari, N. K.; Kim, M. S.; Kim, J. H.; Yu, J. S. Homogeneous deposition of platinum nanoparticles on carbon black for proton exchange membrane fuel cell. *J. Am. Chem. Soc.* **2009**, *131*, 15330–15338.

[5] Liu, M. M.; Zhang, R. Z.; Chen, W. Graphene-supported nanoelectrocatalysts for fuel cells: Synthesis, properties, and applications. *Chem. Rev.* **2014**, *114*, 5117–5160.

[6] Chen, X. M.; Wu, G. H.; Chen, J. M.; Chen, X.; Xie, Z. X.; Wang, X. R. Synthesis of "clean" and well-dispersive Pd nanoparticles with excellent electrocatalytic property on graphene oxide. *J. Am. Chem. Soc.* **2011**, *133*, 3693–3695.

[7] Guo, S. J.; Dong, S. J.; Wang, E. K. Three-dimensional Pt-on-Pd bimetallic nanodendrites supported on graphene nanosheet: Facile synthesis and used as an advanced nanoelectrocatalyst for methanol oxidation. *ACS Nano* **2010**, *4*, 547–555.

[8] Cui, Z. M.; Chen, H.; Zhao, M. T.; Marshall, D.; Yu, Y. C.; Abruña, H.; DiSalvo, F. J. Synthesis of structurally ordered Pt_3Ti and Pt_3V nanoparticles as methanol oxidation catalysts. *J. Am. Chem. Soc.* **2014**, *136*, 10206–10209.

[9] Xia, B. Y.; Wu, H. B.; Li, N.; Yan, Y.; Lou, X. W.; Wang, X. One-pot synthesis of Pt–Co alloy nanowire assemblies with tunable composition and enhanced electrocatalytic properties. *Angew. Chem., Int. Ed.* **2015**, *54*, 3797–3801.

[10] Saleem, F.; Zhang, Z. C.; Xu, B.; Xu, X. B.; He, P. L.; Wang, X. Ultrathin Pt–Cu nanosheets and nanocones. *J. Am. Chem. Soc.* **2013**, *135*, 18304–18307.

[11] Scofield, M. E.; Koenigsmann, C.; Wang, L.; Liu, H. Q.; Wong, S. S. Tailoring the composition of ultrathin, ternary alloy PtRuFe nanowires for the methanol oxidation reaction and formic acid oxidation reaction. *Energy Environ.* Sci, **2015**, *8*, 350–363.

[12] Wang, C.; Daimon, H.; Onodera, T.; Koda, T.; Sun, S. H. A general approach to the size- and shape-controlled synthesis of platinum nanoparticles and their catalytic reduction of oxygen. *Angew. Chem., Int. Ed.* **2008**, *47*, 3588–3591.

[13] Wu, J. B.; Yang, H. Synthesis and electrocatalytic oxygen reduction properties of truncated octahedral Pt_3Ni nanoparticles. *Nano Res.* **2011**, *4*, 72–82.

[14] Qu, L. T.; Liu, Y.; Baek, J. B.; Dai, L. M. Nitrogen-doped graphene as efficient metal-free electrocatalyst for oxygen reduction in fuel cells. *ACS Nano* **2010**, *4*, 1321–1326.

[15] Zhang, W.; Wu, Z. Y.; Jiang, H. L.; Yu, S. H. Nanowire-directed templating synthesis of metal–organic framework nanofibers and their derived porous doped carbon nanofibers

for enhanced electrocatalysis. *J. Am. Chem. Soc.* **2014**, *136*, 14385–14388.

[16] Yang, Z.; Yao, Z.; Li, G. F.; Fang, G. Y.; Nie, H. G.; Liu, Z.; Zhou, X. M.; Chen, X. A.; Huang, S. M. Sulfur-doped graphene as an efficient metal-free cathode catalyst for oxygen reduction. *ACS Nano* **2012**, *6*, 205–211.

[17] Zheng, Y.; Jiao, Y.; Chen, J.; Liu, J.; Liang, J.; Du, A. J.; Zhang, W. M.; Zhu, Z. H.; Smith, S. C.; Jaroniec, M. et al. Nanoporous graphitic-C_3N_4@carbon metal-free electrocatalysts for highly efficient oxygen reduction. *J. Am. Chem. Soc*. **2011**, *133*, 20116–20119.

[18] Lee, K. C.; Zhang, L.; Lui, H. S.; Hui, R.; Shi, Z.; Zhang, J. J. Oxygen reduction reaction (ORR) catalyzed by carbon-supported cobalt polypyrrole (Co-PPy/C) electrocatalysts. *Electrochim. Acta* **2009**, *54*, 4704–4711.

[19] Zhu, Y. S.; Zhang, B. S.; Liu, X.; Wang, D. W.; Su, D. S. Unravelling the structure of electrocatalytically active Fe–N complexes in carbon for the oxygen reduction reaction. *Angew. Chem., Int. Ed*. **2014**, *53*, 10673–10677.

[20] Chen, S.; Bi, J. Y.; Zhao, Y.; Yang, L. J.; Zhang, C.; Ma, Y. W.; Wu, Q.; Wang, X. Z.; Hu, Z. Nitrogen-doped carbon nanocages as efficient metal-free electrocatalysts for oxygen reduction reaction. *Adv. Mater.* **2012**, *24*, 5593–5597.

[21] Shen, A. L.; Zou, Y. Q.; Wang, Q.; Dryfe, R. A. W.; Huang, X. B.; Dou, S.; Dai, L. M.; Wang, S. Y. Oxygen reduction reaction in a droplet on graphite: Direct evidence that the edge is more active than the basal plane. *Angew. Chem., Int. Ed*. **2014**, *53*, 10804–10808.

[22] Houchins, C.; Kleen, G. J.; Spendelow, J. S.; Kopasz, J.; Peterson, D.; Garland, N. L.; Ho, D. L.; Marcinkoski, J.; Martin, K. E.; Tyler, R. et al. U. S. DOE progress towards developing low-cost, high performance, durable polymer electrolyte membranes for fuel cell applications. *Membranes* **2012**, *2*, 855–878.

[23] Chen, J. G. Carbide and nitride overlayers on early transition metal surfaces: Preparation, characterization, and reactivities. *Chem. Rev*. **1996**, 96, 1477–1498.

[24] Liang, C. H.; Ding, L.; Li, C.; Pang, M.; Su, D. S.; Li, W. Z.; Wang, Y. M. Nanostructured WC_x/CNTs as highly efficient support of electrocatalysts with low Pt loading for oxygen reduction reaction. *Energy Environ. Sci*. **2010**, *3*, 1121–1127.

[25] Cui, Z. M.; Gong, C.; Guo, C. X.; Li, C. M. Mo_2C/CNTs supported Pd nanoparticles for highly efficient catalyst towards formic acid electrooxidation. *J. Mater. Chem. A* **2013**, *1*, 1179–1184.

[26] Yin, J.; Wang, L.; Tian, C. G.; Tan, T. X.; Mu, G.; Zhao, L.; Fu, H. G. Low-Pt loaded on a vanadium nitride/graphitic carbon composite as an efficient electrocatalyst for the oxygen reduction reaction. *Chem. Eur. J.* **2013**, *19*, 13979–13986.

[27] Yan, H. J.; Tian, C. G.; Sun, L.; Wang, B.; Wang, L.; Yin, J.; Wu, A. P.; Fu, H. G. Small-sized and high-dispersed WN from $[SiO_4(W_3O_9)_4]^{4-}$ clusters loading on GO-derived graphene as promising carriers for methanol electro-oxidation. *Energy Environ. Sci*. **2014**, *7*, 1939–1949.

[28] Whitby, R. L. D. Chemical control of graphene architecture: Tailoring shape and properties. *ACS Nano* **2014**, *8*, 9733–9754.

[29] Lee, S. H.; Sridhar, V.; Jung, J. H.; Karthikeyan, K.; Lee, Y. S.; Mukherjee, R.; Koratkar, N.; Oh, I. K. Graphene-nanotube-iron hierarchical nanostructure as lithium ion battery anode. *ACS Nano* **2013**, *7*, 4242–4251.

[30] Li, S. S.; Luo, Y. H.; Lv, W.; Yu, W. J.; Wu, S. D.; Hou, P. X.; Yang, Q. H.; Meng, Q. B.; Liu, C.; Cheng, H. M. Vertically aligned carbon nanotubes grown on graphene paper as electrodes in lithium-ion batteries and dye-sensitized solar cells. *Adv. Energy Mater*. **2011**, *1*, 486–490.

[31] Youn, D. H.; Han, S.; Kim, J. Y.; Kim, J. Y.; Park, H.; Choi, S. H.; Lee, J. S. Highly active and stable hydrogen evolution electrocatalysts based on molybdenum compounds on carbon nanotube–graphene hybrid support. *ACS Nano* **2014**, *8*, 5164–5173.

[32] Duan, J. J.; Chen, S.; Chambers, B. A.; Andersson, G. G.; Qiao, S. Z. 3D WS_2 nanolayers@heteroatom-doped graphene films as hydrogen evolution catalyst electrodes. *Adv. Mater.* **2015**, *27*, 4234–4241.

[33] Zhang, L. M.; Lu, Z. X.; Zhao, Q. H.; Huang, J.; Shen, H.; Zhang, Z. J. Enhanced chemotherapy efficacy by sequential delivery of siRNA and anticancer drugs using PEI-grafted graphene oxide. *Small* **2011**, *7*, 460–464.

[34] Li, J.; Tang, W. J.; Huang, J. W.; Jin, J.; Ma, J. T. Polyethyleneimine decorated graphene oxide-supported $Ni_{1-x}Fe_x$ bimetallic nanoparticles as efficient and robust electrocatalysts for hydrazine fuel cells. *Catal. Sci. Technol.* **2013**, *3*, 3155–3162.

[35] Hu, X. G.; Wang, T.; Qu, X. H.; Dong, S. J. *In situ* synthesis and characterization of multiwalled carbon nanotube/Au nanoparticle composite materials. *J. Phys. Chem. B* **2006**, *110*, 853–857.

[36] Cao, X. Y.; Chen, J. J.; Wen, S. H.; Peng, C.; Shen, M. W.; Shi X. Y. Effect of surface charge of polyethyleneimine-modified multiwalled carbon nanotubes on the improvement of polymerase chain reaction. *Nanoscale* **2011**, *3*, 1741–1747.

[37] Yu, D. S.; Dai, L. M. Self-assembled graphene/carbon nanotube hybrid films for supercapacitors. *J. Phys. Chem. Lett.* **2010**, *1*, 467–470.

[38] Ferrari, A. C. Raman spectroscopy of graphene and graphite: Disorder, electron–phonon coupling, doping and nonadiabatic effects. *Solid State Commun.* **2007**, *143*, 47–57.

[39] Stankovich, S.; Dikin, D. A.; Piner, R. D.; Kohlhaas, K. A.; Kleinhammes, A.; Jia, Y. Y.; Wu, Y.; Nguyen, S. T.; Ruo, R. S. Synthesis of graphene-based nanosheets via chemical reduction of exfoliated graphite oxide. *Carbon* **2007**, *45*, 1558–1565.

[40] Zhang, C. H.; Fu, L.; Liu, N.; Liu, M. H.; Wang, Y. Y.; Liu, Z. F. Synthesis of nitrogen-doped graphene using embedded carbon and nitrogen sources. *Adv. Mater.* **2011**, *23*, 1020–1024.

[41] Fernandes, D. M.; Brett, C. M. A.; Cavaleiro, A. M. V. Layer-by-layer self-assembly and electrocatalytic properties of poly(ethylenimine)-silicotungstate multilayer composite films. *J Solid State Electrochem.* **2011**, *15*, 811–819.

[42] Patil, A. J.; Vickery, J. L.; Scott, T. B.; Mann, S. Aqueous stabilization and self-assembly of graphene sheets into layered bio-nanocomposites using DNA. *Adv. Mater.* **2009**, *21*, 3159–3164.

[43] Wu, Z. S.; Yang, S. B.; Sun, Y.; Parvez, K.; Feng, X. L.; Müllen, K. 3D nitrogen-doped graphene aerogel-supported Fe_3O_4 nanoparticles as efficient electrocatalysts for the oxygen reduction reaction. *J. Am. Chem. Soc.* **2012**, *134*, 9082–9085.

[44] Liu, R. L.; Wu, D. Q.; Feng, X. L.; Müllen, K. Nitrogen-doped ordered mesoporous graphitic arrays with high electrocatalytic activity for oxygen reduction. *Angew. Chem., Int. Ed.* **2010**, *122*, 2619–2623.

[45] Tian, G. L.; Zhang, Q.; Zhang, B. S.; Jin, Y. G.; Huang, J. Q.; Su, D. S.; Wei, F. Toward full exposure of "active sites": nanocarbon electrocatalyst with surface enriched nitrogen for superior oxygen reduction and evolution reactivity. *Adv. Funct. Mater.* **2014**, *24*, 5956–5961.

[46] Sun, L.; Tian, C. G.; Fu, Y.; Yang, Y.; Yin, J.; Wang, L.; Fu, H. G. Nitrogen-doped porous graphitic carbon as an excellent electrode material for advanced supercapacitors. *Chem. Eur. J.* **2014**, *20*, 564–574.

[47] He, C. Y.; Meng, H.; Yao, X. Y.; Shen, P. K. Rapid formation of nanoscale tungsten carbide on graphitized carbon for electrocatalysis. *Int. J. Hydrogen Energy* **2012**, *37*, 8154–8166.

[48] Wang, R. H.; Yang, J.; Shi, K. Y.; Wang, B.; Wang, L.; Tian, G. H; Bateer, B.; Tian, C. G.; Shen, P. K.; Fu, H. G. Single-step pyrolytic preparation of Mo_2C/graphitic carbon nanocomposite as catalyst carrier for the direct liquid-feed fuel cells. *RSC Adv.* **2013**, *3*, 4771–4777.

[49] Sun, S. H.; Zhang, G. X.; Gauquelin, N.; Chen, N.; Zhou, J. G.; Yang, S. L.; Chen, W. F.; Meng, X. B.; Geng, D. S.; Banis, M. N. et al. Single-atom catalysis using Pt/graphene achieved through atomic layer deposition. *Sci. Rep.* **2013**, *3*, 1775.

[50] Wang, D. L.; Lu, S. F.; Xiang, Y.; Jiang, S. P. Self- assembly of HPW on Pt/C nanoparticles with enhanced electrocatalysis activity for fuel cell applications. *Appl. Catal. B: Environ.* **2011**, *103*, 311–317.

[51] Cui, G. F.; Shen, P. K.; Meng, H.; Zhao, J.; Wu, G. Tungsten carbide as supports for Pt electrocatalysts with improved CO tolerance in methanol oxidation. *J Power Sources* **2011**, *196*, 6125–6130.

[52] Su, F. B.; Tian, Z. Q.; Poh, C. K.; Wang, Z.; Lim, S. H.; Liu, Z. L.; Lin, J. Y. Pt nanoparticles supported on nitrogen-doped porous carbon nanospheres as an electrocatalyst for fuel cells. *Chem. Mater.* **2010**, *22*, 832–839.

[53] Zhao, S. L.; Yin, H. J.; Du, L.; He, L. C.; Zhao, K.; Chang, L.; Yin, G. P.; Zhao, H. J.; Liu, S. Q.; Tang, Z. Y.; Carbonized nanoscale metal–organic frameworks as high performance electrocatalyst for oxygen reduction reaction. *ACS Nano* **2014**, *8*, 12660–12668.

[54] Kongkanand, A.; Kuwabata, S.; Girishkumar, G.; Kamat, P. Single-wall carbon nanotubes supported platinum nanoparticles with improved electrocatalytic activity for oxygen reduction reaction. *Langmuir* **2006**, *22*, 2392–2396.

[55] Selvarani, G.; Selvaganesh, S. V.; Krishnamurthy, S.; Kiruthika, G. V. M.; Sridhar, P.; Pitchumani, S.; Shukla, A. K. A methanol-tolerant carbon-supported Pt–Au alloy cathode catalyst for direct methanol fuel cells and its evaluation by DFT. *J. Phys. Chem. C* **2009**, *113*, 7461–7468.

[56] Cho, Y. H.; Kim, O. H.; Chung, D. Y.; Choe, H.; Cho, Y. H.; Sung, Y. E. PtPdCo ternary electrocatalyst for methanol tolerant oxygen reduction reaction in direct methanol fuel cell. *Appl. Catal. B: Environ.* **2014**, 154–155, 309–315.

[57] Jeon, M. K.; Lee, K. R.; Lee, W. S.; Daimon, H.; Nakahara, A.; Woo, S. I. Investigation of Pt/WC/C catalyst for methanol electro-oxidation and oxygen electro-reduction. *J. Power Sources* **2008**, *185*, 927–931.